Background Topography Affects the Degree of Three-Dimensionality of Tidal Sand Waves

Janneke Krabbendam[1] , **Abdel Nnafie[1], Bas Borsje[2]** , **and Huib de Swart[1]**

[1]Institute for Marine and Atmospheric Research, Utrecht University, Utrecht, The Netherlands, [2]Faculty of Engineering Technology, Twente University, Enschede, The Netherlands

Abstract Offshore tidal sand waves on the sandy bed of shallow continental shelf seas are more three-dimensional (3D) in some places than others, where 3D refers to a pattern that shows variations in three spatial directions. Such sand waves have crestlines that meander, split or merge. The degree of three-dimensionality seems to vary especially when large-scale bedforms, such as tidal sand banks, are present underneath the sand waves. Understanding this behavior is important for offshore activities, such as offshore windfarm construction or the maintenance of navigation channels. In this study, the degree of three-dimensionality of sand waves at five sites in the North Sea is quantified with a new measure. Results show that tidal sand waves on top of tidal sand banks are more two-dimensional (2D) than those on bank slopes or in open areas. These differences in sand wave pattern are supported by numerical simulations performed with a new long-term sand wave model. The primary cause of these differences is attributed to the deflection of tidal flow over a sand bank, which causes sand wave crests to be more aligned with the bank at its top than at its slopes. It is subsequently made plausible that the different patterns result from the competition between two known mechanisms. These mechanisms are nonlinear interactions between sand waves themselves (SW-SW interactions) and nonlinear interactions between sand banks and sand waves (SB-SW interactions). On bank tops, SB-SW interactions favor a 2D pattern, while SW-SW interactions, which elsewhere produce a 3D pattern, are less effective.

Plain Language Summary Tidal sand waves are rhythmic bedforms that are found at the bottom of shallow seas such as the North Sea. These bedforms have heights of several meters, spacings of hundreds of meters and they can be very mobile. As such, they are important to offshore activities, such as constructing wind farms. Field data indicate that sand waves mainly display a three-dimensional (3D) pattern, with bed level variations in three directions. However, sand waves on tops of sand banks appear to be more 2D (variations in one horizontal and in the vertical direction) than those on slopes. In this study, we analyze bed level data of five areas in the North Sea. The application of a new measure to quantify how 3D a sand wavefield is, confirms that sand waves on bank tops are mostly 2D, while they are 3D on bank slopes or in open areas. The relationship between sand banks and sand wave patterns is investigated with a new sand wave model. Results show that sand banks alter the tidal flow, thereby changing the orientation of the sand waves on top. The emergence of 2D or 3D sand waves is interpreted in terms of two competing nonlinear mechanisms.

1. Introduction

The bathymetry of the world's sandy outer continental shelves is characterized by rhythmic bedforms that have different sizes. Tidal sand banks (sometimes called linear sand ridges) are large-scale features with spacings between successive crests of 2–10 km (Dyer & Huntley, 1999). Tidal sand waves have crest-to-crest distances of several hundreds of meters and are often covered with (mega-)ripples that have spacings ranging from decimeters to tens of meters (McCave, 1971; Terwindt, 1971). Tidal sand waves are the focus of this study. They have typical heights of several meters and migrate with rates of 1–10 m/yr.

Observations show that tidal sand waves are generally three-dimensional features, with bed level variations in three spatial directions. At all five sites in Figure 1, meandering crestlines as well as splitting and merging of crests is observed. However, when sand waves are located on top of a sand bank, a transition from straight crestlines on top to more curved sand waves on the slopes of the bank seems to occur (Figures 1c–1f). These differences in sand wave shape at different locations on the bank also occur on sank banks elsewhere in the world,

Supervision: Abdel Nnafie, Bas Borsje, Huib de Swart
Validation: Janneke Krabbendam
Visualization: Janneke Krabbendam
Writing – original draft: Janneke Krabbendam
Writing – review & editing: Janneke Krabbendam, Abdel Nnafie, Bas Borsje, Huib de Swart

such as on the top of a sand bank in the Beibu Gulf northwest of the South China Sea (Ma et al., 2014) and in the Taiwan Strait (Zhou et al., 2022).

This study addresses the question why crestlines of sand waves on top of sand banks are more straight than those on bank slopes and in open areas. The focus is on the degree of three-dimensionality on the scale of a sand wavefield, which comprises several crest- and troughlines. On this scale, the local tidal and bed characteristics are assumed to be the same. Sand waves with straight crestlines are considered to be two-dimensional, as bed level variations occur predominantly in the vertical direction and in the horizontal direction orthogonal to the crests. In contrast, three-dimensional sand waves also show variations in the horizontal direction along the crests. Such sand waves have crestlines that are curved, meander, split, merge and/or rotate over distances that are small compared to the size of the sand wavefield.

Knowledge about the degree of three-dimensionality of a certain sand wavefield is crucial to determine what type of analysis or modeling approach is needed to simulate their future evolution. The latter is especially important for management purposes. The design, installation and maintenance of cables, pipelines and windmills requires detailed local sand wave information. If sand waves are three-dimensional, bed level measurements at a certain transect will not be representative of the field as a whole, so multiple transects will be needed.

So far, neither field studies nor model studies have investigated the possible connection between large-scale background topography and the degree of three-dimensionality of tidal sand waves. What has been studied is the influence of background topography on sand wave migration: both Ma et al. (2018) and Zhou et al. (2022) observed that sand waves migrate in opposite directions on both sides of a sand bank. Using a numerical 3D model, Leenders et al. (2021) related such bi-directional migration patterns over a sand bank to alterations in residual flow patterns caused by the interaction of the tidal flow with the tidal sand bank. Their morphological model study focused on the initial stage when sand waves have small amplitudes with respect to the water depth and they did not consider the finite-height regime.

Studying the possible connection between background topography and sand wave three-dimensionality requires: (a) a quantitative measure for the degree of three-dimensionality of tidal sand waves and (b) a 3D, process-based, finite-height sand wave model to determine this possible connection. With regard to the first point, in principle a two-dimensional (2D) Fourier analysis could be applied (Damen et al., 2018; Porcile et al., 2020; Van Dijk et al., 2008). This method works well if a surveyed area contains a large number of sand waves, which is frequently not the case. Another complication is that significant variations in sand wave characteristics (i.e., height, length and orientation) occur within the area of interest due to for example, the presence of a sand bank. Venditti et al. (2005) quantified the 'waviness' of dune crests as the ratio of the length of the crestline and the shortest distance between the two endpoints of this crest. However, when many crests merge and split, it is difficult to apply this method, as there is no objective way of separating between different crests. Rubin (2012) and Núñez-González et al. (2021) proposed spatial correlation between various profiles or with a reference profile as a measure to quantify the degree of three-dimensionality. This method works well at the scale of individual sand waves, but as yet, there is no appropriate measure to characterize the three-dimensionality of an entire sand wavefield.

Regarding the three-dimensional modeling of tidal sand waves, Blondeaux and Vittori (2009) studied their finite-height dynamics, using a highly idealized model. They applied a weakly nonlinear analysis and found that resonance effects can lead to the rapid growth of 3D bedforms. This study yielded valuable insights into the formation of 3D patterns, but they only considered a constant water depth and no finite sand wave height was attained. Studies on the long-term, finite-height dynamics of tidal sand waves using numerical models have only been considered in a 2DV context, with models comprising the vertical and the horizontal direction perpendicular to the crests (e.g., Campmans et al., 2018; Krabbendam et al., 2021; Van Gerwen et al., 2018, and references therein). So far, 3D simulations were only obtained for short times, that is, one or two tidal cycles (Leenders et al., 2021).

The previous considerations revealed knowledge gaps that motivate the specific aims of this study, which are twofold: (a) to quantify the degree of three-dimensionality of tidal sand waves observed on different parts of sand banks; and (b) to apply a 3D, finite-height sand wave model to various background topographies and investigate the effect on sand wave three-dimensionality. To address the first objective, five areas in the North Sea are selected. Four of these areas contain sand banks covered with sand waves, and the fifth one consists of sand
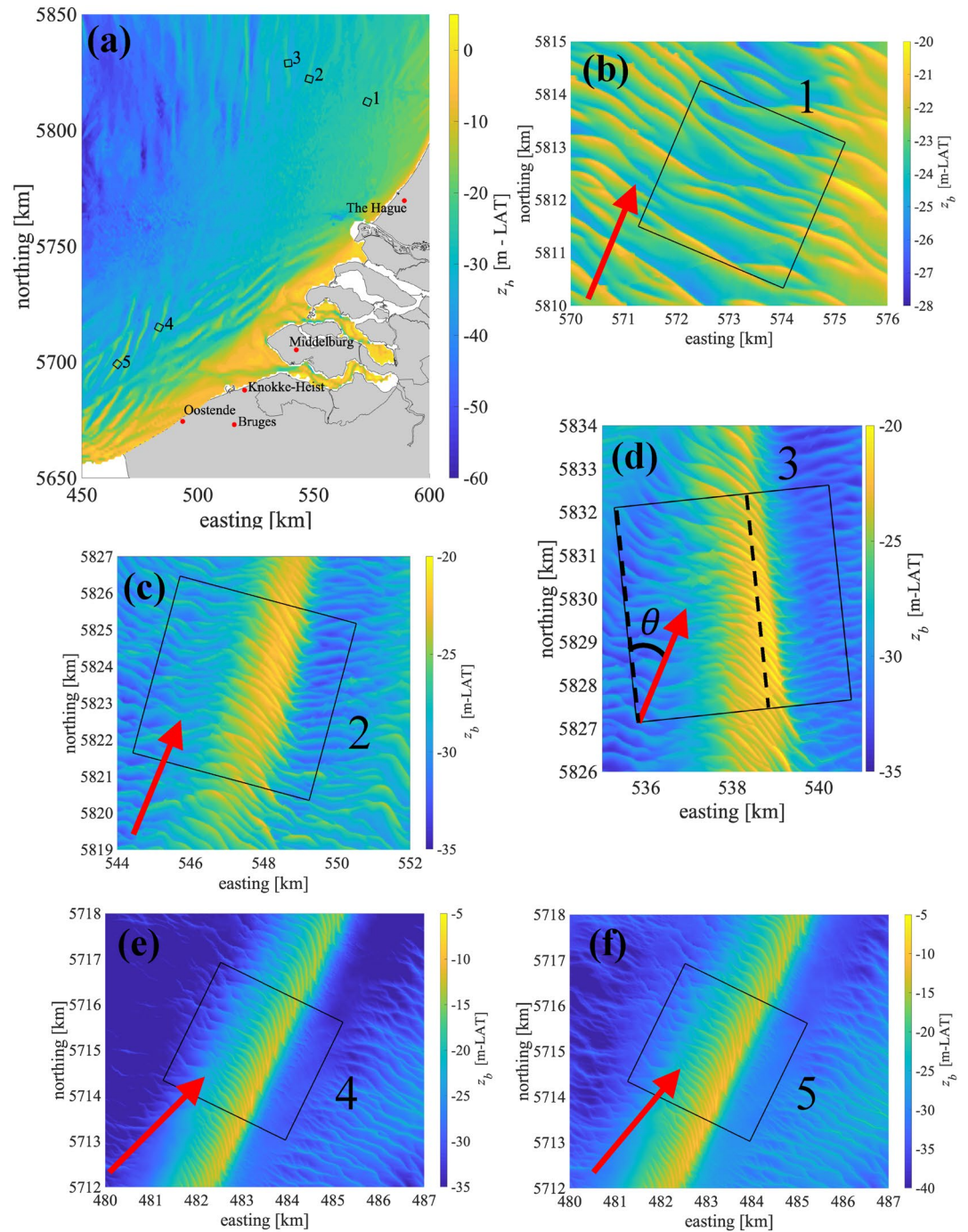
Figure 1. (a) Bathymetry z_b (m-LAT) of the North Sea with the location of the five study areas (European Commission, 2020). Zoom-ins of the bed level in study areas 1–3 are shown in (b–d) (Netherlands Hydrographic Service, 2017) and study areas 4–5 in (e and f) (Flemish Hydrography, 2022). The black boxes within each panel denote the exact edges of the study areas 1–5. The red arrows indicate the mean direction of the M_2-tide obtained from DCSM-Zuno (Zijl, 2013; Zijl et al., 2013). Angle θ (panel (d)) denotes the sand bank orientation, that is, the angle between the bank top and the direction of the domain-averaged tidal current.

waves on a relatively flat background. A new measure to quantify three-dimensionality will be applied to these observations. This measure bares similarities with the one proposed by Núñez-González et al. (2021) but is designed such that it is suitable to quantify the three-dimensionality of a full field. In order to achieve the second objective, a 3D model is presented with which the long-term evolution of tidal sand waves in a 3D domain is

Table 1
Characteristics of Study Areas

		Area 1	Area 2	Area 3	Area 4	Area 5
Mean water depth	D_0	23.6 m LAT	30-23 m LAT	32-22 m LAT	32-12 m LAT	29- 7 m LAT
M_2-amplitude	–	0.6–0.7 m/s	0.6–0.7 m/s	0.6–0.7 m/s	0.7–0.8 m/s	0.7–0.8 m/s
M_2-inclination	–	70°	70°	70°	45°	50°
M_2-ellipticity	–	0.01–0.10	0.01–0.10	0.01–0.10	0.2–0.3	0.2–0.3
Median sand grain size	d_{50}	0.285 mm	0.275 mm	0.290 mm	0.450 mm	0.300–0.350 mm
Sand bank orientation	θ	–	5°	25°	13°	5°
Sand bank height	H_{sb}	–	8 m	10 m	20 m	22 m
Sand bank width	W_{sb}	–	3,100 m	3,000 m	1,900 m	1,600 m

simulated. This model will be used to quantify the effect of different idealized background topographies on the three-dimensionality of sand waves.

Section 2 starts with a description of the five areas selected for quantification of sand wave characteristics, followed by a description of the model, its configuration and the methodology to analyze both observed and modeled sand waves. Results of this analysis are presented in Section 3 and discussed in Section 4. The last section contains the conclusions.

2. Materials and Methods

2.1. Field Data

2.1.1. Study Areas

Field data of sand waves will be analyzed for five study areas. They are all located in the North Sea, where multibeam echosounder data are available (Figure 1a). Area 1 is chosen such that it is not on or directly next to a sand bank (Figure 1b). Areas 2–5 are all located on sand banks (Figures 1c–1f). They are chosen such, that they cover a range of bank shapes and orientations. The bathymetry in Area 1 was obtained in March 2012, Area 2 in July-September 2014 and Area 3 in December 2013, July 2014 and 2015 by the Hydrographic Service of the Royal Netherlands Navy using a multibeam echosounder on a 25 × 25 m grid (Netherlands Hydrographic Service, 2017). The multibeam data in Areas 4 and 5 were obtained by the Flemish Hydrography (2022) on a 10 × 10 m grid. In all areas, the semi-diurnal M_2-tide is the dominant tidal constituent. In Areas 1–3, it has a depth-averaged velocity amplitude of 0.6–0.7 m/s, an inclination of about 70° with respect to the east-west direction and an ellipticity (ratio of the minor and major axis of the ellipse) of 0.01–0.10 (see also Table 1). In the Belgian part, the M_2 current has a slightly larger amplitude of 0.7–0.8 m/s, an ellipticity of 0.2–0.3 and an inclination of 50°. These characteristics are derived from the calibrated tidal model DCSM-ZUNO (for further details see e.g., Zijl, 2013; Zijl et al., 2013). The depth-averaged velocity amplitudes M_4 and M_6 are both 5%–10% of the M_2 amplitude.

In Area 1, the average depth is 23.6 m with respect to the Lowest Astronomical Tide (LAT) (Table 1). The sand waves are covered with (mega-)ripples with heights of up to 0.5 m and wavelengths of up to 20 m, with average values of 0.2 and 10 m, respectively (Van Dijk & Kleinhans, 2005). The median grain size d_{50} is similar in Areas 1–3, with $d_{50} = 285$ μm, $d_{50} = 275$ μm and $d_{50} = 290$ μm, respectively (Damen et al., 2018). Areas 2 and 3 are characterized by sand banks, with heights H_{sb} of 8 and 10 m and crests positioned at depths of 23 and 22 m LAT, respectively. The sand bank in Area 2 has a 5° anticlockwise orientation θ with respect to the tidal current. In Area 3, the orientation is 25° anticlockwise (Figure 1d). Both banks span a width W_{sb} of approximately 3 km in the direction across the bank, with the steepest slopes facing in the direction of the flood current (indicated by the red arrows in Figure 1). The sand banks in Areas 4 and 5 have heights H_{sb} of 20 and 22 m, with the crests located at a water depth of 12 and 7 m LAT, respectively. These banks span a width of 1.5–2.0 km and the steepest slopes are found in the direction of the flood current. These sand banks have anticlockwise orientations $\theta = 13°$ and 5° with respect to the long axis of the tidal ellipse. The median sand grain size found in Areas 4 and 5 is approximately 450 μm (Reubens et al., 2009) and 300–350 μm (Deleu et al., 2004), respectively.
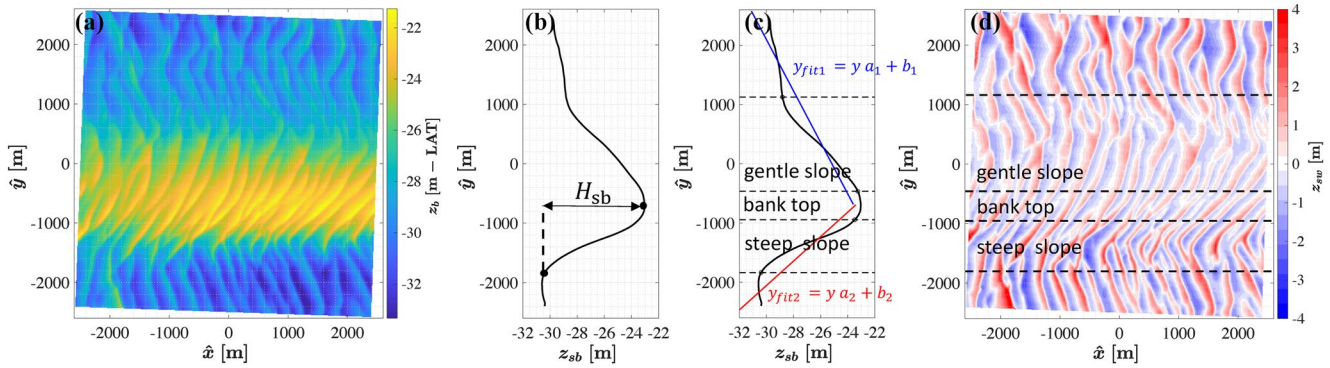
Figure 2. (a) Bed level data $z_b(\hat{x}, \hat{y})$ (m-LAT) obtained in Area 2 where the sand bank aligns with the $\hat{x}$-axis. (b) Average sand bank profile $z_{sb}(\hat{y})$ (m). (c) Sand wave topography $z_{sw}(\hat{x}, \hat{y})$ (m) is defined as $z_b(\hat{x}, \hat{y}) - z_{sb}(\hat{y})$. (d) Average sand bank profile z_{sb} (m) with linear fits y_{fit1} of the gentle slope (blue) and y_{fit2} of the steep slope (red) of the bank. Black dashed lines distinguish the five subdomains of the sand bank based on whether the value of local slope $\frac{dz_{sb}}{d\hat{y}}$ is $\geq 0.9a_1$ or $\geq 0.9a_2$, where a_1 and a_2 are the overall slopes obtained from y_{fit1} and y_{fit2}, respectively.

2.1.2. Analysis of Bed Level Data

The multi-beam data $z_b(t, X, Y)$ (m-LAT) are interpolated on a $\hat{x} - \hat{y}$-grid with 10 m spacings in both directions and a 5×5 km (Areas 2 and 3) or 3×3 km (Areas 4 and 5) extent. In this frame, the $\hat{x}$-axis aligns with the sand bank (Figure 2a). In order to remove the sand bank signal from the data, the bed level is averaged over a number of different transects $\hat{y}_j =$ constant to obtain the average sand bank profile $z_{sb}(\hat{y})$ (m):

$$z_{sb}(t, \hat{y}_j) = \frac{1}{N_j} \sum_{i=1}^{N_j} z_b(t, \hat{x}_i, \hat{y}_j), \tag{1}$$

with N_j the total number of gridpoints $\hat{x}_i$ along transects $\hat{y}_j =$ constant. The $\hat{x} - \hat{y}$-grid is chosen such that the variance of $z_{sb}(\hat{y})$ is maximum. This sand bank profile is subsequently subtracted from the bed level data to obtain the topography $z_{sw}(t, \hat{x}, \hat{y}) = z_b(t, \hat{x}, \hat{y}) - z_{sb}(t, \hat{y})$ (Figures 2b and 2c), that represents tidal sand waves. In principle, z_{sw} also contains megaripples and even smaller bedforms, but the resolution of the original bathymetry data (25×25 m for Areas 1–3 and 10×10 m for Areas 4–5) is such that only sand waves are resolved.

To study the various parts of a sand bank, subdomains are considered: the top, the steep and gentle slopes and the two remote flat parts. The key parameters that determine the borders between the subdomains are the overall slopes a_1 and a_2 of each side of the sand bank. The sand bank top is defined as the local maximum of z_{sb} and separates the domain into a steep and gentle side. Linear fits of $z_{sb}(t, \hat{y}_j)$ y_{fit1} and y_{fit2} are obtained for both sides, resulting in average slopes a_1 and a_2 (Figure 2d), blue and red lines, respectively). If local minima of z_{sb} are determined, the linear fit is applied to z_{sb} between this local minimum and the top. All $\hat{y}_j$ where the local slope $\frac{dz_{sb}}{d\hat{y}} \geq 0.9 \; a_1$ or a_2 are defined as the sloping part of the sand bank. The rest of the domain is classified as "bank top" or "flat," depending on whether $\hat{y}_j$ is located between two slope domains or not.

Then, for each subdomain, the $(\hat{x}, \hat{y})$-axes are rotated in the horizontal plane to new (x, y)-axes, such that the majority of the crestlines aligns with the y-axis in the new frame (Figure 3a). Next, $z_{sw}(x, y)$ is averaged along a number of different transects $x_m =$ constant to obtain the average sand wave profile $z_{sw,2D}(x)$ (m):

$$z_{sw,2D}(x_m) = \frac{1}{N_m} \sum_{n=1}^{N_m} z_{sw}(x_m, y_n), \tag{2}$$

with N_m the number of gridpoints y_n along a transect $x_m =$ constant. The rotation is done over the angle for which the variance of $z_{sw,2D}(x)$ is maximum. Finally, $z_{sw,2D}(x)$ is subtracted from $z_{sw}(x, y)$ to obtain the deviation from the average sand wave profile $z'_{sw}(x, y)$. The above procedure is illustrated in Figures 3b–3g, which shows two examples of weakly and strongly meandering sand waves. Figure S1 in Supporting Information S1 demonstrates how this procedure applies to observed sand waves.
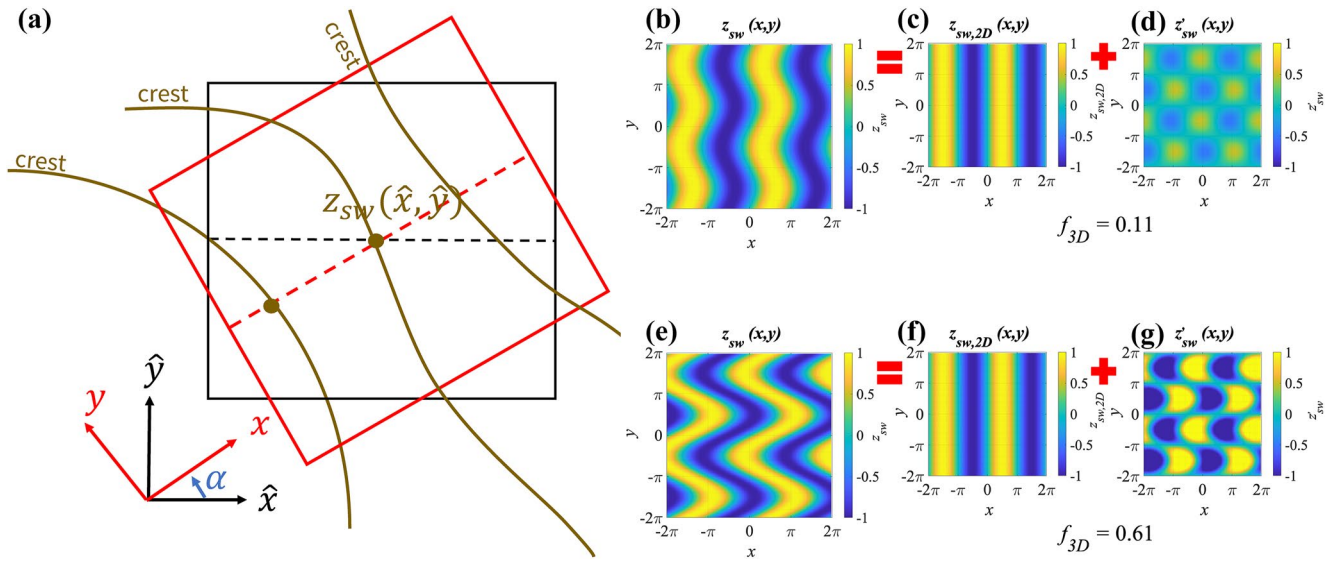
Figure 3. (a) Schematic view of the rotation of the $(\hat{x}, \hat{y})$-grid (in which the $\hat{x}$ axis aligns with the sand bank) to the (x, y)-grid within each subdomain. For each subdomain, the rotation angle α is chosen such that the majority of the local crestlines of sand waves align with the y-axis. Two examples of weakly (b–d) and strongly (e–g) meandering sand waves illustrate how the bed level of an artificial sand wavefield z_{sw} is decomposed into $z_{sw,2D}$ and z'_{sw}. The corresponding value of the degree of three-dimensionality f_{3D} is also indicated.

After performing these steps, all the ingredients are present to define a measure for the degree of three-dimensionality f_{3D} of the sand wavefield. For each subdomain, f_{3D} is computed as follows:

$$f_{3D} = \frac{\sigma_{3D}^2}{\sigma_{3D}^2 + \sigma_{2D}^2} \tag{3}$$

with σ_{3D}^2 the variance of z'_{sw}

$$\sigma_{3D}^2 = \frac{1}{N_{3D}} \sum_{m=1}^{N_n} \sum_{n=1}^{N_m} \left(z'_{sw}(x_m, y_n) \right)^2, \tag{4}$$

and σ_{2D}^2 the variance of $z_{sw,2D}$

$$\sigma_{2D}^2 = \frac{1}{N_n} \sum_{m=1}^{N_n} \left(z_{sw,2D}(x_m) \right)^2. \tag{5}$$

In these equations, N_m is the number of y-points along a transect x_m = constant and N_n is the number of x-points along a transect y_n = constant. The total number of points in the 3D-domain $N_{3D} = \sum_{m=1}^{N_{y,max}} N_m$, with $N_{y,max}$ the total number of transects y_n = constant. The value of f_{3D} lies between 0 and 1 and indicates how well $z_{sw,2D}$ represents z_{sw}. A value close to 0 means that σ_{2D}^2 is large compared to σ_{3D}^2 and most of the bed level variance is captured by $z_{sw,2D}$. Consequently, the bed is considered to be almost two-dimensional. When f_{3D} approaches 1, most of the bed level variance is in z'_{sw} and the bed is fully three-dimensional. To demonstrate how f_{3D} captures the shape of sand wave crestlines, two examples of weakly and strongly meandering sand wave crestlines are shown in Figures 3b–3g as well as the corresponding values of f_{3D} (further details of these examples are presented in Supporting Information S1).

2.2. Model

2.2.1. Equations of Motion

To address the second aim, this study uses the numerical morphological model Delft3D (Lesser et al., 2004) in a configuration based on Borsje et al. (2013, 2014), Krabbendam et al. (2021), and Leenders et al. (2021). The model equations are solved in (X, Y, σ)-equations, with (X, Y) the coordinates along the two horizontal dimensions. The vertical coordinate is $\sigma = \frac{z - \zeta}{D + \zeta}$ with ζ the free surface elevation with respect to reference level $z = 0$ and D the water depth below this level. In the horizontal direction, the model has lengths L_X and L_Y (Figure 4a), whereas σ
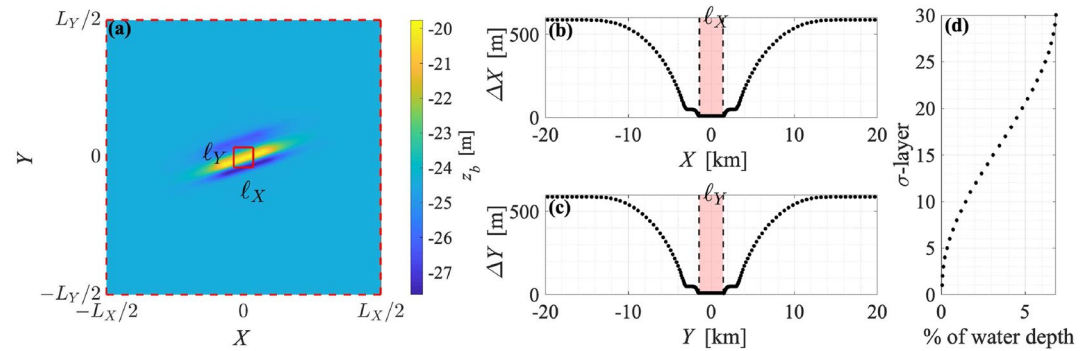
Figure 4. (a) Model domain as seen from the top in (X, Y)-coordinates for the sand bank configuration, with horizontal lengths L_X and L_Y. The red, dashed lines denote the location of the open boundaries of the full computational domain. The area of interest (red box) has lengths (ℓ_X, ℓ_Y) and corresponds to the part of the domain with the highest horizontal resolution. The colors represent the initial bed level $z_{b0}(X, Y) = -D_0 + z_{sb}(X, Y) + h(X, Y)$, with D_0 the still water depth, $z_{sb}(X, Y)$ the sand bank profile and $h(X, Y)$ random, small-amplitude bed perturbations. Grid sizes ΔX (b) and ΔY (m) (c) as a function of X and Y (km). The red shaded area corresponds to the area of interest. (d) Percentage of the water depth in each σ-layer.

is -1 at the bed and 0 at the free surface. In this domain, the 3D shallow water equations are solved in the module FLOW. At the open boundaries ($X = -L_X/2$, $X = L_X/2$, $Y = -L_Y/2$ and $Y = L_Y/2$, denoted by the red, dashed lines), the incoming tidal waves are imposed using the weakly reflective Riemann invariants R (Verboom & Slob, 1984). These are a linear combination of the water level and the depth-averaged velocity component normal to the open boundary. Turbulence is computed using the $k - \varepsilon$-model and roughness is imposed with a Nikuradse roughness length k_s.

The output of FLOW is used as input for the module SED, where the bed load and suspended load transport are computed with the equations of Van Rijn (1993). The bed load transport is corrected for slope effects (Bagnold, 1966), both in the transverse and longitudinal direction of the flow. These corrections contain the user-defined bed slope parameters α_{bn} and α_{bs}, respectively.

The changes in bed level z_b are computed in the module MOR, using the divergence of the sediment transport through the sediment continuity equation. A morphological acceleration factor (MORFAC) is included to speed up the bed level changes, as these are assumed to happen on a much larger timescale (years) than hydrodynamic changes (hours). The new bed level is input for the module FLOW in the next timestep.

2.2.2. Model Configuration

The model settings are summarized in Table 2. The model configuration is based on the characteristics of Area 1 in the Dutch part of the North Sea (Figure 1b). The domain has lengths $L_X = L_Y = 40$ km in the horizontal directions. The grid sizes decrease from $(\Delta X, \Delta Y) = (590, 590)$ m at the boundaries to $(\Delta X, \Delta Y) = (10, 10)$ m in the middle of the domain (Figures 4b and 4c). This middle part where $(\Delta X, \Delta Y) = (10, 10)$ m has lengths $\ell_X = \ell_Y = 3$ km and is considered to be the area of interest. Around this area, there is a ring where $(\Delta X, \Delta Y) = (50, 50)$ m, so that the hydrodynamic and bed level information in this area are resolved with a high resolution. In the vertical direction, the water column is divided into 30 non-equidistant σ-layers, where the percentage of the water depth in one layer increases from 0.05% at the bed to 6.8% at the surface (Figure 4d).

To set proper boundary conditions, the 3D grid is nested in the calibrated tidal North Sea model DCSM-ZUNO (for further details see e.g., Zijl et al., 2013). The resulting water levels and normal depth-averaged velocities are combined into Riemann M_2, M_4, M_6, and M_0-amplitudes and phases using T-Tide (Pawlowicz et al., 2002).

As initial bathymetry, three different background topographies are considered: (a) a flat bed; (b) the average sand bank profile of Area 2 and (c) the average sand bank profile of Area 3 (Table 3). The flat topography has a still

Table 2
Model Settings

Parameter	Symbol	Value	Dimension
Domain sizes	L_x, L_y	40, 40	km
Sizes of area of interest	ℓ_x, ℓ_y	3, 3	km
Undisturbed water depth	D_0	24.42	m
Roughness length	k_s	0.0944	m
Median sand grain size	d_{50}	0.285	mm
Longitudinal bed slope parameter	α_{bs}	3	–
Transverse bed slope parameter	α_{bn}	1.5	–
Hydrodynamic time step	Δt	12	s
Horizontal grid spacing	$\Delta x, \Delta y$	10, 10	m
Number of σ-layers	-	30	–
Morphological acceleration factor	MORFAC	2,000	–

Table 3
Overview of Model Experiments

Run	Background topography
1	flat, $D_0 = 24.42$ m
2	z_{sb} of Area 2, $\theta = 5°$
3	z_{sb} of Area 3, $\theta = 25°$

water depth of $D_0 = 24.42$ m, which is the average water depth in Area 1 with respect to mean sea level. The topography with a sand bank results from adding the average sand bank profile z_{sb} from Areas 2 and 3 to D_0 (Figure 4a). The imposed sand banks have anticlockwise angles of $\theta = 5°$ and $25°$ with respect to the modeled tidal current, which are representative for the situations in Areas 2 and 3, respectively.

To each of these topographies, random, small-amplitude bed perturbations $h(X, Y)$ are added. These bed perturbations are generated with the white-noise generator built-in MATLAB and have a maximum amplitude of $0.005D_0$ in the area of interest. Outside of the area of interest, $h(X, Y)$ decreases gradually to zero through multiplication with tapered cosine window.

The roughness length k_s is based on the dimensions of megaripples in Area 1, which have heights of several decimeters and wavelengths of 10–20 m. Using the formulation of Van Rijn (1993), this results in a value of $k_s = 0.0944$ m (Krabbendam et al., 2021). The median grain size d_{50} is set to 285 µm, following the median grain size in Area 1 given by Damen et al. (2018). The longitudinal slope parameter is $\alpha_{bs} = 3$ and the transverse slope parameter $\alpha_{bn} = 1.5$. The timestep is $\Delta t = 12$ s and MORFAC is set to 2,000. The first two tidal cycles comprise the spin-up phase, during which no bed level changes take place.

2.2.3. Design of Experiments

The configuration with the flat bed was selected as the default setting (Run 1). From this simulation, it was ascertained that the modeled tidal current axis makes a 13° angle with the X-axis. Therefore, all values of θ are anticlockwise with respect to this 13°. Next, the background topography was changed to the average sand bank profiles of Areas 2 and 3 (Runs 2 and 3). Throughout these experiments, all other model settings were kept constant. An overview of the model experiments is presented in Table 3.

2.2.4. Analysis of Model Results

At each time step, the model output was analyzed in the same way as described in Section 2.1.2. In order to address the second objective, wave height H was computed to determine whether the modeled sand waves reach a finite height and a quasi-equilibrium state. The wave height is defined as the vertical distance between a crest and subsequent trough along transects with $y_n =$ constant. The values of H were averaged over each subdomain in Runs 2 and 3 and over the whole domain in Run 1. These domain averages are denoted with square brackets (i.e., $[H]$). The equilibrium time scale t_{eq} is defined as $[H](t_{eq}) = 0.98[H](t = 300 \text{ yr})$. After that, the degree of three-dimensionality f_{3D} was computed for each time step and for each (sub-)domain, using Equations 3–5.

3. Results

3.1. Field Data

Figure 5 shows the sand wave topography $z_b(\hat{x}, \hat{y})$ (m) in Areas 1–5. In these plots, the $\hat{x}$-axis is aligned with the sand bank. The black dashed lines indicate where the areas are split into subdomains. The average sand bank profile $z_{sb}(\hat{y})$ (m-LAT) is shown on the lower horizontal axis in panels (b), (d), (f), and (h) and the variable along the vertical axis is $\hat{y}$ (m). The upper horizontal axis denotes the value of f_{3D} for the sand waves in each of the subdomains. When the background topography is relatively flat, the sand waves are three-dimensional, with $f_{3D} = 0.7$ (Figure 5b). In Areas 2–5, f_{3D} reaches a minimum on the bank tops, with values ranging between 0.2 and 0.5, these sand waves can thus considered to be two-dimensional. On the slopes on either side, the sand waves are more 3D than those on the top, as f_{3D} increases to 0.7–0.8. There is no clear difference between the two slopes, although in Areas 2, 3, and 5, the gentle side value is slightly higher. These results support the hypothesis that the degree of three-dimensionality depends on the background topography. This will be further investigated by analyzing the output of the numerical model.

3.2. Model Results

3.2.1. Finite-Height Sand Waves

The time evolution of the domain-averaged wave height $[H](t)$ (m) of Run 1 is shown in blue in Figure 6a. After $t_{eq} = 230$ years, the sand waves saturate toward an equilibrium height $[H]_{eq}$ of about 7.0 m. At this point, the tidal sand waves have a value of $f_{3D} = 0.5$–0.6 (red scatters in (a)). Panels (b–e) show the modeled bed level $z_b(t, x, y)$
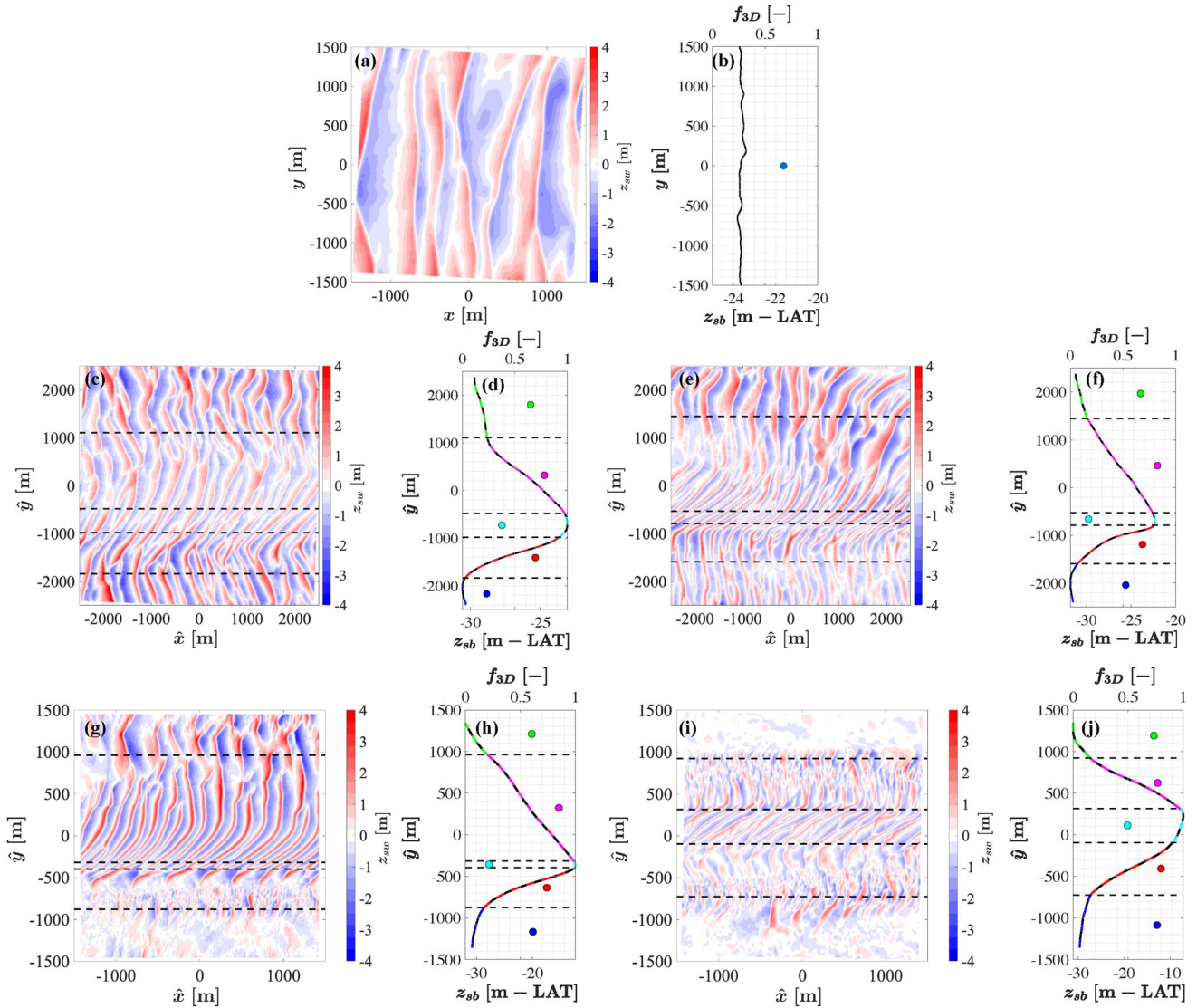
Figure 5. (a), (c), (e), (g), (i) Sand wave topography $z_{sw}(\hat{x}, \hat{y})$ (m) for Areas 1–5, respectively. (b), (d), (f), (h), and (j) average sand bank profile $z_{sb}(\hat{y})$ (m-LAT) on the lower horizontal axis and $\hat{y}$ on the vertical axis. The upper horizontal axis denotes the value of f_{3D} for the sand waves in each of the subdomains.

(m) at different times during the simulation. Comparing the bed levels at $t = 200$ yr and $t = 300$ yr suggests that the changes in [H] after $t = t_{eq}$ are mainly the result of merging crests. From these results, it can be concluded that the modeled sand waves evolve toward a quasi-equilibrium state and that this model is suited to investigate the finite-height behavior of sand waves. Therefore, as a next step, a sand bank is added to the background topography.

3.2.2. Degree of Three-Dimensionality

The time evolution of the domain-averaged wave height [H] (m) for Run 2 is shown in Figure 7a, where the colored scatters correspond to different parts of the sand bank. The time series of the degree of three-dimensionality f_{3D} in the same areas is shown in panel (b). Initially $f_{3D} = 1$ and it slowly decreases. The lowest values of f_{3D} are found at the top of the bank ($f_{3D} = 0.3$). On the sloping parts of the bank, f_{3D} is about 0.5–0.6. Snapshots of the sand wave topography $z_{sw}(\hat{x}, \hat{y})$ of Run 2 at several times are shown in panels (c–e), where the black dashed lines indicate the borders between the different subdomains. On the steep slope, the sand waves change their orientation downslope causing f_{3D} to be higher than at the top, and on the gentle slope, there are several locations where crests merge. These subdomains slightly shift during the simulation. These shifts are caused by small changes in the average sand bank profile z_{sb} during the simulation (Figure 7f) and result in small variations in f_{3D}.
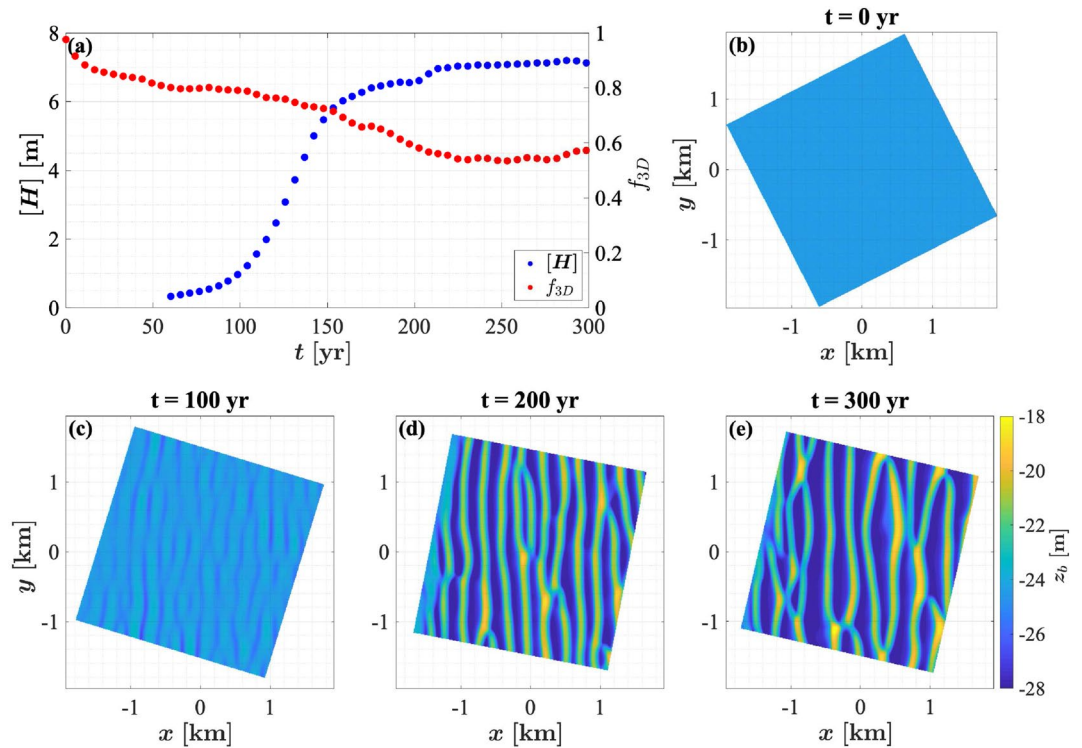
Figure 6. Domain-averaged sand wave height $[H](t)$ (m, blue) and degree of three-dimensionality f_{3D} (red) (a) as function of morphological simulation time t (yr) for Run 1. (b–e) Bed level $z_b(t, x, y)$ (m) at $t = 0$ yr, $t = 100$ yr, $t = 200$ yr and $t = 300$ yr, respectively.

The sand bank in Run 3 is adjusting itself in the sense that the sand bank top becomes higher and narrower (Figure 8f). The orientation of the sand bank does not change. This results in a narrowing of the bank top subdomain (Figures 8d and 8e), with a value of f_{3D} of approximately 0.1. When the width of the top is smaller than
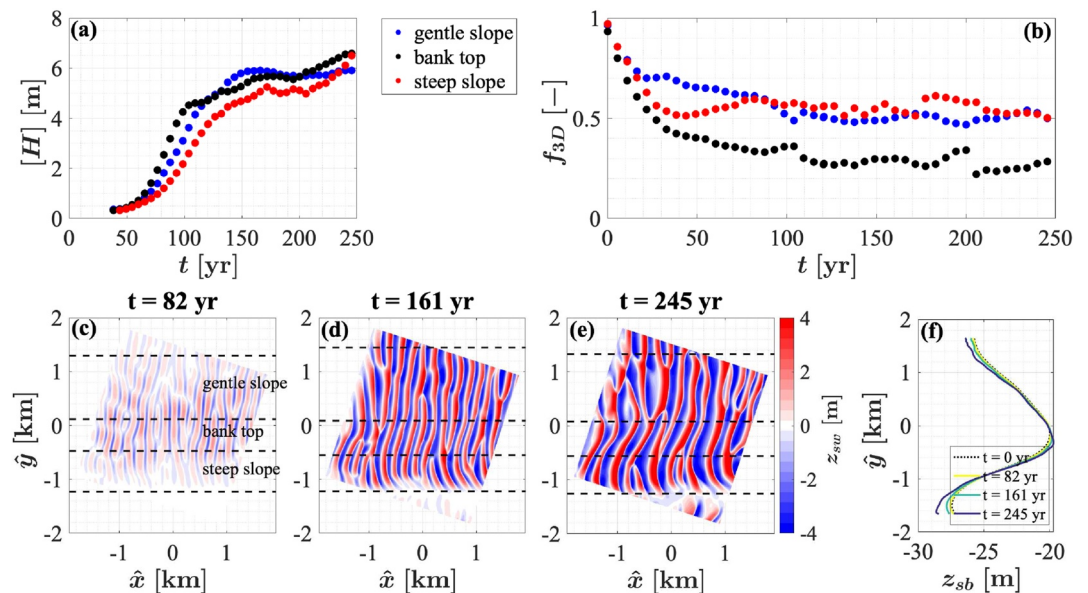

Figure 7. Domain-averaged sand wave height $[H](t)$ (m) (a) and degree of three-dimensionality $f_{3D}(t)$ (b) for Run 2, where the different colors correspond to different parts of the sand bank. (c–e) Sand wave topography $z_{sw}(t, \hat{x}, \hat{y})$ (m) for Run 2 is shown for three times during the simulation. The black dashed lines distinguish the subdomains at each time step. (f) Average sand bank profile $z_{sb}(t, \hat{y})$ (m) at $t = 0$ yr (black dotted), at $t = 82$ yr (yellow), $t = 161$ yr (green) and $t = 245$ yr (blue).
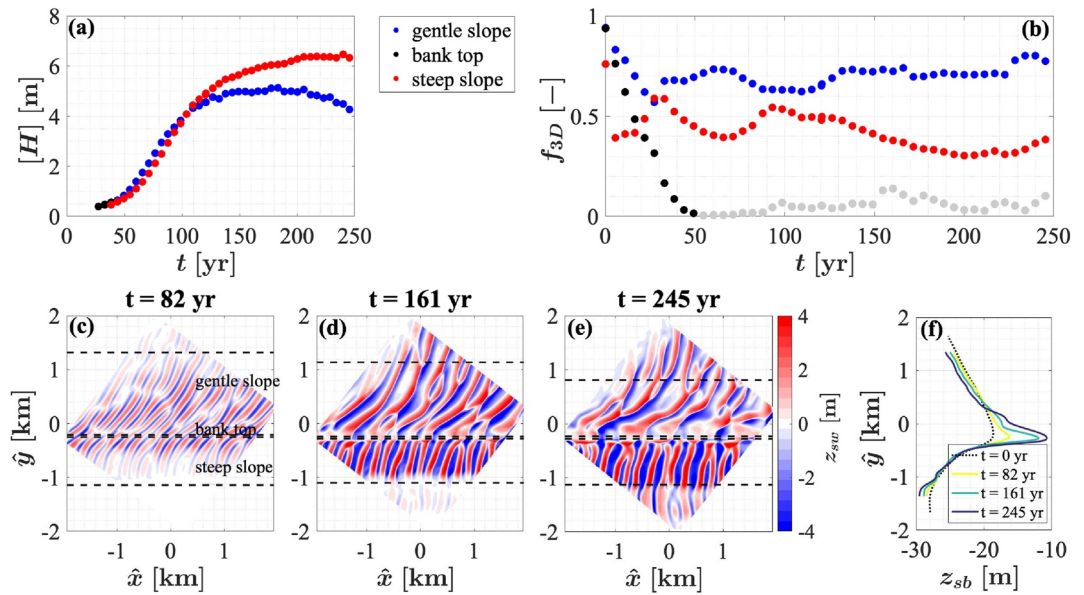
Figure 8. Domain-averaged sand wave height $[H](t)$ (m) (a) and degree of three-dimensionality $f_{3D}(t)$ (b) for Run 3, where the different colors correspond to different parts of the sand bank. The black scatters correspond to the bank top subdomain, but they are plotted in gray if the width of the top subdomain is smaller than 100 m. (c–e) Sand wave topography $z_{sw}(t, \hat{x}, \hat{y})$ (m) for Run 3 is shown for three times during the simulation. The black dashed lines distinguish the subdomains at each time step. (f) Average sand bank profile $z_{sb}(t, \hat{y})$ (m) at $t = 0$ yr (black dotted), $t = 82$ yr (yellow), $t = 161$ yr (green) and $t = 245$ yr (blue).

100 m, f_{3D} is plotted in gray in (b). On the slopes of the bank, f_{3D} is about 0.3–0.7. Just as in Run 2, the sand waves on the steep slope change their orientation rapidly downslope. The gentle slope is characterized by many locations where crests merge or split in time.

4. Discussion

In this study, the degree of three-dimensionality (expressed by a new measure f_{3D}) of tidal sand waves observed in five offshore areas with different background bathymetries was quantified. One of these areas (Area 1) consists of tidal sand waves on a relatively flat background bathymetry, while in other areas (Areas 2–5), sand waves are located on tidal sand banks. Results show that sand waves are relatively more three-dimensional on flat bathymetries and on slopes of sand banks than those on bank tops. The differences in sand wave shape depending on background bathymetry are supported by numerical simulations performed with a new 3D sand wave model. Below, possible physical mechanisms responsible for these differences are described (Section 4.1). Also, results from additional simulations using different sand bank characteristics (orientation and width) are presented. In Sections 4.2 and 4.3, the measure used to quantify the degree of three-dimensionality (f_{3D}) and the design of the sand wave model are discussed.

4.1. Physical Mechanisms Causing 2D and 3D Sand Wave Patterns

A plausible explanation for the fact that sand waves are overall 3D features, except at the top of tidal sand banks, is found in the competition between two known nonlinear mechanisms that affect the evolution of sand waves. These two mechanisms are nonlinear interactions between sand waves themselves (Blondeaux & Vittori, 2009) and nonlinear interactions between a sand bank and sand waves (Komarova & Newell, 2000). To explain these mechanisms, the initial formation of sand waves is discussed first.

Tidal sand waves form spontaneously as a result of tide-topography interaction. It involves a hydrodynamic part, which causes the formation of residual currents on either side of the crests of bottom undulations, and a morpho-dynamic part that leads to the growth of the bottom undulations. The hydrodynamic mechanism is equivalent to that described by Zimmerman (1981) for the case of tidal currents near headlands (the latter can be seen as the

horizontal equivalences of sand waves). First, note that tidal currents become weaker toward the bottom, because of bed resistance. This vertical velocity shear implies that the tide possesses vorticity, which is positive (clockwise) during flood and negative during ebb.

Next, consider a tidal current moving over an initially small bottom undulation (see Figure S3a in Supporting Information S1). At any fixed vertical level, mass conservation causes velocity to be largest above the crests of the bottom undulation and smallest in the troughs. So, as is illustrated in Figure S3b of Supporting Information S1, there are horizontal gradients in the vorticity, and thus also in the transport of tidal vorticity by the tidal current. Divergence of the vorticity transport subsequently results in a local build-up of vorticity. For example, during flood, the vorticity transport is convergent on the downstream side of the crest of the bottom undulation. Interestingly, during both flood and ebb tidal vorticity and tidal velocity change sign, but the vorticity transport does not. Consequently, averaged over a tidal cycle, residual vorticity occurs on either side of the crests of bottom undulation. As is shown in Figure S3c of Supporting Information S1, the residual currents that are associated with the residual vorticity cells in the vertical plane point from troughs to crests.

The morphodynamic part of the initial formation mechanism follows arguments in Hulscher et al. (1993). Key is that sand transport is a nonlinear function of local near-bed velocity. Thus, the joint action of tidal and residual currents causes sand transport, during both flood and ebb, to be relatively large on the stoss side of the crest (residual current acts with the tidal current) and relatively weak on the lee side (residual current acts against the tidal current). This results in net convergence of sand transport at the crest, so the bottom undulation grows.

The arguments above hold for any bottom undulation. As the domain has no horizontal boundaries, the actual bottom consists of a superposition of Fourier modes, also referred to as bottom modes, each having its own wave vector $\vec{\kappa}$. So, starting from a bed with small, random bottom perturbations, all these bottom modes will be present and evolve in time. Their growth rates, however, are not the same. In particular, modes with small wavenumbers $|\vec{\kappa}|$ (long waves) grow relatively slowly, because bed changes result from divergence of sediment transport, which is weak when crests are spaced far apart. The behavior of modes with large $|\vec{\kappa}|$ (short waves) is, besides the mechanism described above, also significantly affected by divergence of bed slope-induced transport (sediment prefers to move downhill), which even causes growth rates to become negative for very large $|\vec{\kappa}|$. Thus, a maximum growth rate is to be expected for intermediate $|\vec{\kappa}|$ and that mode is called the initially most preferred mode (IMP-sand wave mode). Model experiments indeed confirm this picture (see the review by Besio et al. (2008)) and show that the IMP-mode resembles observed sand waves: it has a wavelength of several hundreds of meters and its crests are oriented perpendicular to the long axis of the depth-averaged tidal current.

The initial growth mechanism described above only holds for the initial formation of sand waves, when the amplitudes of the bottom modes are still small. On the longer term, this is no longer the case and nonlinear interactions between different bottom modes take place, which affect the bottom pattern formation. Nonlinear sand wave–sand wave interactions (SW-SW-interactions) were first discussed in Blondeaux and Vittori (2009). They consider the evolution of tidal sand waves in the absence of a tidal sand bank, and show that effective growth of a 3D bottom pattern results from the presence of resonant wave triads that involve the IMP-sand wave mode (with wave vector $\vec{\kappa}_1 = (\alpha, 0)$) and two other modes, with wave vecors $\vec{\kappa}_2 = \left(\frac{1}{2}\alpha, \gamma\right)$ and $\vec{\kappa}_3 = \left(\frac{1}{2}\alpha, -\gamma\right)$. Clearly, the latter two modes have crests that make nonzero angles with those of the IMP-sand wave mode when $\gamma \neq 0$. The involved modes satisfy the resonance condition $\vec{\kappa}_1 = \vec{\kappa}_2 + \vec{\kappa}_3$, which means that quadratic nonlinear interactions between any two modes will transfer energy to the third mode, and not outside the triad. Thus, such triads are so efficient because they involve the IMP mode, and thereby receive a large input of energy through the linear growth mechanism, and because this energy remains within the triad. Resonant triads also occur in many other branches of physics (see e.g., Craik, 1988). Blondeaux and Vittori (2009) demonstrate that the wavenumber γ that defines the most efficient wave triad depends on the ellipticity of the tide. For large tidal ellipticity 3D bottom patterns evolve the fastest. For weaker tidal ellipticity the most efficient wave triad is for $\gamma = 0$, but many triads with nonzero γ are almost as efficient and thus the bottom pattern will be 3D. In a later study, Rubin (2012) arrives at the same conclusion; he describes the emergence of 3D bottom patterns as being due to a lack of "physical coupling along the crests of the bedform" (here: the IMP-sand wave mode).

When a sand bank is present, such a physical coupling will arise, because the sand bank affects the tidal flow. In particular, conservation of mass forces the cross-bank component of the tidal velocity to increase when directed upslope and to decrease when directed downslope (Dyer & Huntley, 1999; Huthnance, 1973, 1982). As a result,
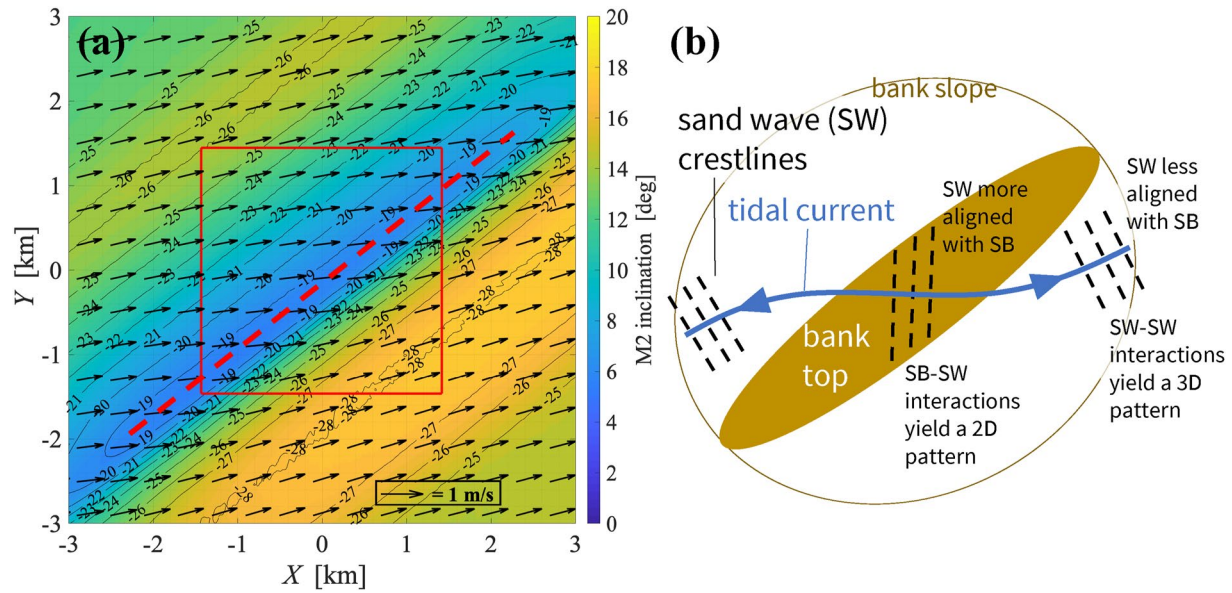
Figure 9. (a) Vector plot of the long axis of the depth-averaged M$_2$-current in Run 3, where the colors denote the inclination of the long axis with respect to the *X*-axis (degrees). The black labeled lines are the depth contours and the area of interest is indicated by the red box. The red dashed line indicates the position of the bank top. (b) Schematic view that illustrates the deflection of the tidal current (blue) over a tidal sand bank (SB, brown) and the corresponding orientation of the tidal sand wave crests (SW, black, dashed lines).

the angle between the long axis of the depth-averaged tidal current and the sand bank is larger at the top than on its slopes (Figure 9a). As the initially most preferred sand wave mode (IMP mode) has crests that are perpendicular to the tidal current, it follows that crests of sand waves are more aligned with the bank on its top, and less so on its slopes (Figure 9b). This property is visible in Figure 5 and in Figures 7 and 8, where the crestlines of the sand waves display an S-shape over the bank. The change in orientation of sand waves on a bank top as a result from deflected currents over a bank was also observed in the area of the Taiwan Banks in the South China Sea (Zhou et al., 2022).

Now consider the situation at the top of the sand bank. This area has a small width, in the sense that only a few sand waves fit into it. We hypothesize that the limited width hampers SW-SW interactions. The reason is that the two bottom modes with which the IMP-sand wave mode interacts, have wavelengths in the direction of the tidal current that are twice as large as that of the IMP-mode. Such subharmonic modes do not fit well into this area and are therefore not efficiently excited. At the same time, there is a mechanism on the top of the sand bank that favors the sand wavefield to be 2D. This mechanism, described by Komarova and Newell (2000), involves nonlinear interactions between modulated sand waves (i.e., with slightly varying wavelengths) and the tidal sand bank. They are referred to as sandbank-sand wave interactions (SB-SW interactions). Again, they occur between three modes that form a resonant triad, but here the three modes are 2D, so their crests are aligned. The first mode is the tidal sand bank, with wavenumber $\kappa_1 = \Delta\kappa$. The other two are Fourier modes with wavenumbers $\kappa_2 = \kappa_{sw} - \frac{1}{2}\Delta\kappa$ and $\kappa_{sw} + \frac{1}{2}\Delta\kappa$, where $\Delta\kappa \ll \kappa_{sw}$ and κ_{sw} is the primary wavenumber of the sand waves; when superimposed these modes describe the modulated sand wavefield. Indeed, these modes satisfy the resonance condition $\kappa_1 = \kappa_2 + \kappa_3$. This mechanism is thus efficient when the crests of sand waves and the sand bank are aligned.

The situation on the slopes of the sand bank is quite different from that on its top. These slopes generally span a larger width than the bank tops, so we expect the mechanism of SW-SW-interactions described by Blondeaux and Vittori (2009) to be effective here. Moreover, the crests of sand waves on the slope are not aligned with the bank. The SB-SW-mechanism of Komarova and Newell (2000) is thus expected to be less effective. The combined effect results in a more 3D sand wave pattern on the slopes of the bank.

To gain more insight into the effects of the sand bank characteristics on sand wave patterns, additional simulations were performed in which, relative to the bank imposed in Run 2: (a) the sand bank was rotated clockwise ($\theta = -13°$) and anti-clockwise ($\theta = 25°$) and (b) the width W_{sb} was decreased and increased with 20%. For larger anticlockwise angles between the sand bank and the long axis of the tidal current ($\theta = 25°$), the deflection of the tidal current over
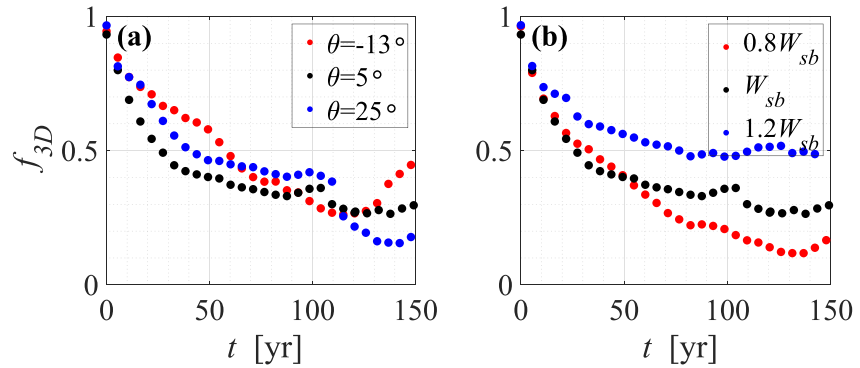
Figure 10. Time series of degree of three-dimensionality f_{3D} of sand waves at the bank top for sand banks with a different orientation θ (a) and a different width across the bank top W_{sb} (b). The black scatters ($\theta = 5°$ and W_{sb}) correspond to the bank imposed in Run 2.

the sand bank is stronger than for smaller angles. As a result, the sand waves on the top of sand banks are more aligned with the bank and become more 2D (Figure 10a). A clockwise orientation of the bank with respect to the tide (which rarely occurs in the Northern Hemisphere (Dyer & Huntley, 1999)), results in larger angles between the crestlines and the bank and more 3D sand waves. A decrease in the width of the bank, while keeping all other bank characteristics the same, means that sand wave crests maintain the same orientation, but the bank top area reduces. Therefore, the resonant nonlinear interactions with other sand waves are further suppressed, causing the sand waves to be more 2D (Figure 10b). The sand wave topographies obtained with these additional simulations are shown in Figures S4 and S5 of Supporting Information S1. These additional simulations support our hypothesis. However, to prove that the mechanisms of Komarova and Newell (2000) and Blondeaux and Vittori (2009) cause sand wave patterns to be more 2D on bank tops would require additional analysis with a more idealized model, which is outside the scope of this study.

4.2. The Measure of Three-Dimensionality f_{3D}

The degree of three-dimensionality f_{3D} was applied to sand wave fields at different subdomains of a sand bank. The borders of these subdomains were defined by setting a criterion based on the local bed slope. The application of another criterion (the bank top subdomain is the region where $z_{sb} \geq \min(z_{sb}) + 0.9H_{sb}$), changes the borders between the subdomains, but yields a qualitatively similar outcome: sand waves on the top of banks are more 2D than those on bank slopes (Figure S6 in Supporting Information S1). We also tested the use of an alternative measure for three-dimensionality, viz. that of Núñez-González et al. (2021). Their measure yields information at the level of individual sand waves, but when viewed at the scale of the sand wavefield, it shows a similar pattern (Figure S7 in Supporting Information S1). Hence, f_{3D} is a suitable measure to quantify the degree of three-dimensionality at the scale of a sand wavefield.

Alternatively, a measure based on the crestlines could be defined, such as the sinuosity or the amount of splitting and merging events, similar to the proposed method of Venditti et al. (2005). Recently, several methods to automatically detect crestlines have been developed (Cassol et al., 2022; Lebrec et al., 2022) with which this would be possible. However, the challenge remains to determine where a crestline starts and ends.

4.3. Remarks About the Design of the Sand Wave Model

Starting from small random bottom perturbations, the 3D sand wave model was able to simulate the evolution toward finite-height tidal sand waves. They reach an average height of 7.0 m in approximately 220 years with a value of f_{3D} between 0.5 and 0.6. For comparison, the observed average sand wave height in Area 1 is 2.0 m with $f_{3D} = 0.7$. This indicates that the model overestimates the sand wave height, while f_{3D} is quite close to the observed value. The fact that modeled heights of sand waves are too large is a common characteristic of all long-term numerical sand wave models (Campmans et al., 2018; Krabbendam et al., 2021; Van Gerwen et al., 2018). The source of this behavior is not yet clear. However, there are some simplifications within the model: wind, waves, storms, biology and geology (erodible sediment layer thickness) are missing and tidal forcing is simplified. There are indications from highly idealized model studies that wind, waves, storms and biology can affect the finite sand wave height (Campmans et al., 2018; Damveld et al., 2020), but this remains a topic for future research.

Finally, note that to keep simulation time below reasonable limits, the numerical model parameters (grid size, morphological acceleration factor, time step) were optimized. This means that if the grid size, the morphological acceleration factor or the time step are reduced, or the number of σ-layers increased, the modeled sand wave height will change slightly, but the overall sand wave behavior remains the same (Figures S8 and S9 in Supporting Information S1). In the current settings, 100 years of simulation time takes about 1 month on an intel Xeon 2.10 GHz Linux computer. Several 2DV finite-height studies have suggested calibrations to obtain a better match with observations (Campmans et al., 2022; Krabbendam et al., 2021), but the long simulation time restricts the number of runs that can be done.

5. Conclusions

Using a new measure for the degree of three-dimensionality, analysis of bathymetry data of tidal sand waves in an area without sand banks, as well as in four areas on sand banks in the North Sea shows that sand waves on the top of sand banks are more two-dimensional than those on the slopes or in open areas. These differences in pattern are supported by numerical simulations performed with a new 3D sand wave model, which is able to simulate long-term finite-height sand waves. Previous studies have shown that bedforms tend to become three-dimensional due to nonlinear resonant interactions and when there are no constraints in the direction of sediment transport. However, in case that a sand bank is present, the latter deflects the tidal flow. This changes the orientation of sand waves at the bank tops such that the sand waves become more aligned with the sand bank. We hypothesize that, as a result, nonlinear resonant interactions between sand waves themselves are less effective, while nonlinear interactions between sand bank and sand waves are enhanced. Consequently, sand waves on a bank top become more 2D than sand waves on bank slopes.

Data Availability Statement

The Dutch bathymetric data from the Netherlands Hydrographic Service (2017) are available through http://opendap.deltares.nl/thredds/catalog/opendap/hydrografie/surveys/catalog.html. The Belgian bathymetric data from the Flemish Hydrography (2022) are available through https://bathy.agentschapmdk.be/spatialfusionviewer/mapViewer/map.action. The modeled and observed bed levels as well as the Matlab scripts to analyze these are available on https://doi.org/10.6084/m9.figshare.24065163.v1 and https://doi.org/10.6084/m9.figshare.24065148.v1 respectively.

References

Bagnold, R. A. (1966). An approach to the sediment transport problem from general physics. In *US Geological Survey Professional Paper 422-I*. U.S. Government Printing Office. https://doi.org/10.3133/pp422I

Besio, G., Blondeaux, P., Brocchini, M., Hulscher, S. J. M. H., Idier, D., Knaapen, M. A. F., et al. (2008). The morphodynamics of tidal sand waves: A model overview. *Coastal Engineering*, *55*(7–8), 657–670. https://doi.org/10.1016/j.coastaleng.2007.11.004

Blondeaux, P., & Vittori, G. (2009). Three-dimensional tidal sand waves. *Journal of Fluid Mechanics*, *618*, 1–11. https://doi.org/10.1017/S0022112008004138

Borsje, B. W., Kranenburg, W. M., Roos, P. C., Matthieu, J., & Hulscher, S. J. M. H. (2014). The role of suspended load transport in the occurrence of tidal sand waves. *Journal of Geophysical Research: Earth Surface*, *119*(4), 701–716. https://doi.org/10.1002/2013JF002828

Borsje, B. W., Roos, P. C., Kranenburg, W. M., & Hulscher, S. J. M. H. (2013). Modeling tidal sand wave formation in a numerical shallow water model: The role of turbulence formulation. *Continental Shelf Research*, *60*, 17–27. https://doi.org/10.1016/j.csr.2013.04.023

Campmans, G. H. P., Roos, P. C., De Vriend, H. J., & Hulscher, S. J. M. H. (2018). The influence of storms on sand wave evolution: A nonlinear idealized modeling approach. *Journal of Geophysical Research: Earth Surface*, *123*(9), 2070–2086. https://doi.org/10.1029/2018JF004616

Campmans, G. H. P., Van Dijk, T. A. G. P., Roos, P. C., & Hulscher, S. J. M. H. (2022). Calibration and validation of two tidal sand wave models: A case study of the Netherlands continental shelf. *Journal of Marine Science and Engineering*, *10*(12), 1902. https://doi.org/10.3390/jmse10121902

Cassol, W. N., Daniel, S., & Guilbert, É. (2022). An approach for the automatic characterization of underwater dunes in fluviomarine context. *Geosciences*, *12*(2), 89. https://doi.org/10.3390/geosciences12020089

Craik, A. D. D. (1988). *Wave interactions and fluid flows*. Cambridge University Press. https://doi.org/10.1017/CBO9780511569548

Damen, J. M., Van Dijk, T. A. G. P., & Hulscher, S. J. M. H. (2018). Spatially varying environmental properties controlling observed sand wave morphology. *Journal of Geophysical Research: Earth Surface*, *123*(2), 262–280. https://doi.org/10.1002/2017JF004322

Damveld, J. H., Borsje, B. W., Roos, P. C., & Hulscher, S. J. M. H. (2020). Biogeomorphology in the marine landscape: Modelling the feedbacks between patches of the polychaete worm Lanice conchilega and tidal sand waves. *Earth Surface Processes and Landforms*, *45*(11), 2572–2587. https://doi.org/10.1002/esp.4914

Deleu, S., Van Lancker, V., Van den Eynde, D., & Moerkerke, G. (2004). Morphodynamic evolution of the kink of an offshore tidal sandbank: The Westhinder Bank (Southern North Sea). *Continental Shelf Research*, *24*(15), 1587–1610. https://doi.org/10.1016/j.csr.2004.07.001

Dyer, K. R., & Huntley, D. A. (1999). The origin, classification and modelling of sand banks and ridges. *Continental Shelf Research*, *19*(10), 1285–1330. https://doi.org/10.1016/S0278-4343(99)00028-X

European Commission. (2020). EMODnet Map Viewer - DTM Tiles. Retrieved from https://emodnet.ec.europa.eu/geoviewer/

Flemish Hydrography. (2022). Bathymetrisch grid. Retrieved from https://bathy.agentschapmdk.be/spatialfusionviewer/mapViewer/map.action

Hulscher, S. J. M. H., de Swart, H. E., & de Vriend, H. J. (1993). The generation of offshore tidal sand banks and sand waves. *Continental Shelf Research*, *13*(11), 1183–1204. https://doi.org/10.1016/0278-4343(93)90048-3

Huthnance, J. M. (1973). Tidal current asymmetries over the Norfolk Sandbanks. *Estuarine and Coastal Marine Science*, *1*(1), 89–99. https://doi.org/10.1016/0302-3524(73)90061-3

Huthnance, J. M. (1982). On one mechanism forming linear sand banks. Estuarine. *Coastal and Shelf Science*, *14*(1), 79–99. https://doi.org/10.1016/S0302-3524(82)80068-6

Komarova, N. L., & Newell, A. C. (2000). Nonlinear dynamics of sand banks and sand waves. *Journal of Fluid Mechanics*, *415*, 285–321. https://doi.org/10.1017/S0022112000008855

Krabbendam, J. M., Nnafie, A., De Swart, H. E., Borsje, B. W., & Perk, L. (2021). Modelling the past and future evolution of tidal sand waves. *Journal of Marine Science and Engineering*, *9*(10), 1071. https://doi.org/10.3390/jmse9101071

Lebrec, U., Riera, R., Paumard, V., O'Leary, M. J., & Lang, S. C. (2022). Automatic mapping and characterisation of linear depositional bedforms: Theory and application using bathymetry from the North West Shelf of Australia. *Remote Sensing*, *14*(2), 280. https://doi.org/10.3390/rs14020280

Leenders, S., Damveld, J. H., Schouten, J., Hoekstra, R., Roetert, T. J., & Borsje, B. W. (2021). Numerical modelling of the migration direction of tidal sand waves over sand banks. *Coastal Engineering*, *163*, 103790. https://doi.org/10.1016/j.coastaleng.2020.103790

Lesser, G. R., Roelvink, J. A., Van Kester, J. A. T. M., & Stelling, G. S. (2004). Development and validation of a three-dimensional morphological model. *Coastal Engineering*, *51*(8–9), 883–915. https://doi.org/10.1016/j.coastaleng.2004.07.014

Ma, X., Li, J., & Yan, J. (2018). Tide-induced bedload transport pathways in a multiple-sand-ridge system offshore of Hainan Island in the Beibu Gulf, northwest South China Sea. *Earth Surface Processes and Landforms*, *43*(13), 2738–2753. https://doi.org/10.1002/esp.4428

Ma, X., Yan, J., & Fan, F. (2014). Morphology of submarine barchans and sediment transport in barchans fields off the Dongfang coast in Beibu Gulf. *Geomorphology*, *213*, 213–224. https://doi.org/10.1016/j.geomorph.2014.01.010

McCave, I. N. (1971). Sand waves in the North Sea off the coast of Holland. *Marine Geology*, *10*(3), 199–225. https://doi.org/10.1016/0025-3227(71)90063-6

Netherlands Hydrographic Service. (2017). Hydrographic Surveys. Retrieved from http://opendap.deltares.nl/thredds/catalog/opendap/hydrografie/surveys/catalog.html

Núñez-González, F., Hesse, D., Ettmer, B., Gutierrez, R. R., & Link, O. (2021). Development and validation of a novel metric for describing the three-dimensionality of bed forms. *Geomorphology*, *390*, 107856. https://doi.org/10.1016/j.geomorph.2021.107856

Pawlowicz, R., Beardsley, B., & Lentz, S. (2002). Classical tidal harmonic analysis including error estimates in MATLAB using T_TIDE. *Computers & Geosciences*, *28*(8), 929–937. https://doi.org/10.1016/S0098-3004(02)00013-4

Porcile, G., Blondeaux, P., & Colombini, M. (2020). Starved versus alluvial river bedforms: An experimental investigation. *Earth Surface Processes and Landforms*, *45*(5), 1229–1239. https://doi.org/10.1002/esp.4800

Reubens, J., Eede, S. V., & Vincx, M. (2009). Monitoring of the effects of offshore wind farms on the endobenthos of soft substrates: Year-0 Bligh Bank and Year-1 Thorntonbank. In S. Degraer & R. Brabant (Eds.), *Offshore wind farms in the Belgian part of the North Sea: State of the art after two years of environmental monitoring* (pp. 59–91). Royal Belgian Institute of Natural Sciences, Management Unit of the North Sea Mathematical Models, Marine Ecosystem Management Unit.

Rubin, D. M. (2012). A unifying model for planform straightness of ripples and dunes in air and water. *Earth-Science Reviews*, *113*(3–4), 176–185. https://doi.org/10.1016/j.earscirev.2012.03.010

Terwindt, J. H. J. (1971). Sand waves in the Southern Bight of the North Sea. *Marine Geology*, *10*(1), 51–67. https://doi.org/10.1016/0025-3227(71)90076-4

Van Dijk, T. A. G. P., & Kleinhans, M. G. (2005). Processes controlling the dynamics of compound sand waves in the North Sea, Netherlands. *Journal of Geophysical Research*, *110*(F4), 1–15. https://doi.org/10.1029/2004JF000173

Van Dijk, T. A. G. P., Lindenbergh, R. C., & Egberts, P. J. P. (2008). Separating bathymetric data representing multiscale rhythmic bed forms: A geostatistical and spectral method compared. *Journal of Geophysical Research*, *113*(F4), F04017. https://doi.org/10.1029/2007JF000950

Van Gerwen, W., Borsje, B. W., Damveld, J. H., & Hulscher, S. J. M. H. (2018). Modelling the effect of suspended load transport and tidal asymmetry on the equilibrium tidal sand wave height. *Coastal Engineering*, *136*, 56–64. https://doi.org/10.1016/j.coastaleng.2018.01.006

Van Rijn, L. C. (1993). *Principles of sediment transport in rivers, estuaries and coastal seas*. Aqua Publications.

Venditti, J. G., Church, M., & Bennett, S. J. (2005). On the transition between 2D and 3D dunes. *Sedimentology*, *52*(6), 1343–1359. https://doi.org/10.1111/j.1365-3091.2005.00748.x

Verboom, G. K., & Slob, A. (1984). Weakly-reflective boundary conditions for two-dimensional shallow water flow problems. *Advances in Water Resources*, *7*(4), 192–197. https://doi.org/10.1016/0309-1708(84)90018-6

Zhou, J., Wu, Z., Zhao, D., Guan, W., Cao, Z., & Wang, M. (2022). Effect of topographic background on sand wave migration on the eastern Taiwan Banks. *Geomorphology*, *398*, 108030. https://doi.org/10.1016/j.geomorph.2021.108030

Zijl, F. (2013). *Development of the next generation Dutch Continental Shelf Flood Forecasting models, memo, 1205989-003-ZKS-0002*. Deltares.

Zijl, F., Verlaan, M., & Gerritsen, H. (2013). Improved water-level forecasting for the Northwest European Shelf and North Sea through direct modelling of tide, surge and non-linear interaction. *Ocean Dynamics*, *63*(7), 823–847. https://doi.org/10.1007/s10236-013-0624-2

Zimmerman, J. T. F. (1981). Dynamics, diffusion and geomorphological significance of tidal residual eddies. *Nature*, *290*(5807), 549–555. https://doi.org/10.1038/290549a0